THE JOURNAL OF PHYSICAL CHEMISTRY A

Article

Cite This: J. Phys. Chem. A 2018, 122, 3837−3849

pubs.acs.org/JPCA

Model Behavior: Characterization of Hydroxyacetone at the Air−Water Interface Using Experimental and Computational Vibrational Sum Frequency Spectroscopy

Brittany P. Gordon,[†] Frederick G. Moore,[‡] Lawrence F. Scatena,[†] Nicholas A. Valley,[†,§] Sumi N. Wren,[†,∥] and Geraldine L. Richmond*[,†]

[†]Department of Chemistry, University of Oregon, 1253 University of Oregon, Eugene, Oregon 97403, United States

[‡]Department of Physics, Whitman College, Walla Walla, Washington 99362, United States

[§]Department of Science and Mathematics, California Northstate University College of Health Sciences, Rancho Cordova, California 95670, United States

[∥]Department of Air Quality Process Research, Environment and Climate Change Canada (ECCC), Toronto, Ontario M3H 5T4, Canada

Supporting Information

ABSTRACT: Small atmospheric aldehydes and ketones are known to play a significant role in the formation of secondary organic aerosols (SOA). However, many of them are difficult to experimentally isolate, as they tend to form hydration and oligomer species. Hydroxyacetone (HA) is unusual in this class as it contributes to SOA while existing predominantly in its unhydrated monomeric form. This allows HA to serve as a valuable model system for similar secondary organic carbonyls. In this paper the surface behavior of HA at the air−water interface has been investigated using vibrational sum frequency (VSF) spectroscopy and Wilhelmy plate surface tensiometry in combination with computational molecular dynamics simulations and density functional theory calculations. The experimental results demonstrate that HA has a high degree of surface activity and is ordered at the interface. Furthermore, oriented water is observed at the interface, even at high HA concentrations. Spectral features also reveal the presence of both *cis* and *trans* HA conformers at the interface, in differing orientations. Molecular dynamics results indicate conformer dependent shifts in HA orientation between the subsurface (∼5 Å deep) and surface. Together, these results provide a picture of a highly dynamic, but statistically ordered, interface composed of multiple HA conformers with solvated water. These results have implications for HA's behavior in aqueous particles, which may affect its role in the atmosphere and SOA formation.

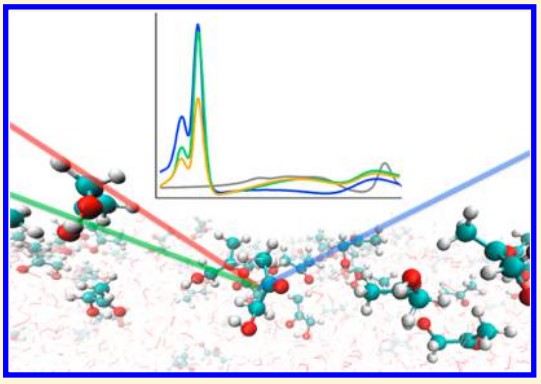

1. INTRODUCTION

Small oxygenated volatile organic compounds (OVOCs) are ubiquitous in the atmosphere and of great importance in secondary organic aerosol (SOA) formation.[1−13] Yet, there still exist many uncertainties in the specific roles these small organics play in the formation and consequent fate of SOA.[13−17] Water-soluble aldehydes and ketones have been of particular interest, due in part to their tendency to hydrate and oligomerize upon partitioning into the aqueous phase.[13,18−35] Indeed, some of these organics (e.g., glyoxal,[24] methylglyoxal,[18,36] and pyruvic acid[31,37]) are unusual in that their most stable forms in the aqueous phase are geminal diols, which are generally less stable than unhydrated carbonyls. This tendency to form higher molecular weight species leads to higher concentrations within aqueous aerosols than is predicted from Henry's law alone.[1,11,16,17,19,38,39] Once in the particle phase, these species participate in further oligomerization and oxidation reactions, thereby contributing to increased SOA mass, referred to as aqueous phase processing.[8,18,20−24,27,30,31,34,39−45]

Since aerosols have a large surface area to volume ratio, the surface chemistry of these particles can greatly influence their behavior and have far-reaching effects on the environment.[1,46−51] For example, it has been shown that surface interactions can strongly affect the adsorptions of atmospheric gases to aqueous surfaces.[47] Gaining a better understanding of the aerosol air−water interface is an ongoing area of research.[13,36,45,52−55] However, experiments with carbonyl species are often complicated because subsequent to purification (often, a challenge itself), exposure to water results

Received: February 2, 2018
Revised: March 21, 2018
Published: April 2, 2018

DOI: 10.1021/acs.jpca.8b01193
J. Phys. Chem. A 2018, 122, 3837−3849

in an equilibrium shift into a continuum of hydration species, effectively generating a mixed organic system.[18] Temperature, pH, and salinity can drive the hydration to favor one species, but each of these perturbations also has its own effect on the system and particularly on surface behavior.[18,26,31,52,56] Furthermore, the ratio of different hydration species can be depth dependent.[36] Thus, a small carbonyl that is surface active, atmospherically relevant, and unfavorable for either hydration or dimerization would serve as an invaluable model system for studying how these organics behave at aerosol interfaces.

Hydroxyacetone (HA) is just such a system. HA has been the focus of work in many fields due to its physiological, industrial, and astrochemical significance.[1,57−68] This work focuses on HA's role as a prevalent semivolatile atmospheric hydroxycarbonyl. HA has been observed experimentally in situ with other secondary organics known to contribute to SOA formation.[1] Some studies have identified HA as the most abundant carbonyl species in aqueous SOA.[1] HA is rather unique among these types of secondary organics because while HA can also hydrate to form a geminal diol, this hydration has been shown to be unfavorable. Glushonok et al. demonstrated that in the aqueous phase 96−98% of HA exists in the unhydrated, monomeric carbonyl form with no covalently bonded dimeric or polymeric species detected.[68]

Although HA has been thoroughly examined in the gas, condensed (aqueous), and solid phases using multiple spectroscopic techniques,[1,57−68] little to no work has been done on the surface chemistry of HA at liquid interfaces. To elucidate the behavior and conformational distribution of HA at the air−water interface, this study uses vibrational sum frequency (VSF) spectroscopy, a surface specific technique, in combination with surface tensiometry and computational methodologies. Of particular focus is the conformer distribution and hydrogen-bonding environment of HA at the air−water interface, as these properties have been shown to be phase dependent.[59,61−63,65−67] By characterizing the HA−neat water system, this work lays the groundwork for future studies on more complicated mixed organic systems.

2. EXPERIMENTAL AND THEORETICAL METHODS

2.1. Vibrational Sum Frequency Spectroscopy. Vibrational sum frequency (VSF) spectroscopy is a nonlinear technique that is inherently surface selective and provides a convolution of orientation and population information for anisotropically ordered, surface-active, noncentrosymmetric molecules. This technique has been used extensively for the study of liquid interfaces.[69−81] A sum frequency signal is generated by overlapping a visible beam and a tunable-frequency IR beam in time and space, producing a third beam at the sum of the incident frequencies. The intensity of the VSF signal is proportional to the absolute square of the nonlinear second-order macroscopic susceptibility ($\chi^{(2)}$). The second-order susceptibility has both resonant ($\chi^{(2)}_{R\nu}$) and nonresonant ($\chi^{(2)}_{NR}$) components. The resonant portion of the VSF response contains information about both the *population* and *orientation* of species adsorbed at an interface. To deconvolve these numerous contributions, VSF spectra are fit using eq 1:[82,83]

$$\chi^{(2)} = \chi^{(2)}_{NR} e^{i\psi} + \sum_{\nu} \int_{-\infty}^{\infty} \frac{A_\nu e^{i\varphi_\nu} e^{-(\omega_L - \omega_\nu/\Gamma_\nu^2)^2}}{\omega_L - \omega_{IR} + i\Gamma_L} d\omega_L \quad (1)$$

The first term in eq 1 is the nonresonant susceptibility, described by an amplitude and phase, ψ. The second term defines contributions from the resonant second-order susceptibility ($\chi^{(2)}_{R\nu}$) as the summation over all VSF-active resonant vibrational modes. Included in this resonant second-order susceptibility are the transition strengths (A_ν), phases (φ_ν), and terms describing the homogeneous line widths of the individual molecular transitions (Γ_L) as well as inhomogeneous broadenings (Γ_ν). The Lorentzian, resonant modes, and IR frequencies are defined as ω_L, ω_ν, and ω_{IR}, respectively. Equation 1 is utilized for the fitting equation and spectral analysis of the VSF data, using mode-specific fixed Lorentzian widths (based on reported vibrational lifetimes of the specific transition)[84−88] for the CH (2 cm^{-1}), coordinated OH and C═O (5 cm^{-1}), and "free" OH (12 cm^{-1}).

VSF spectra discussed within are obtained using either the *ssp* or *sps* polarization scheme, where the three letters denote the polarizations of the sum frequency, visible, and IR beams, respectively. The *ssp* scheme probes molecular dipole components perpendicular to the air−water interface while the *sps* scheme probes components parallel to the interface.

2.2. Laser System. The picosecond laser system used to obtain the VSF results discussed here has been reported,[36,89,90] such that only a brief description is necessary for this work. A sum frequency (SF) beam is generated by overlapping a fixed visible beam (12 500 cm^{-1}) with a tunable IR beam at the air−water interface in a copropagating geometry at 45° and 60°, respectively, relative to the surface normal. The SF beam leaving the interface is collected using a curved mirror set at its focal length and directed into a thermoelectrically cooled CCD camera (Pixas, Princeton Instruments). A LabView program measures the CCD intensity while scanning (3 cm^{-1} wavelength step) over the tunable IR range between 4000 and 1200 cm^{-1}. The nonresonant SF response of an uncoated gold substrate was measured daily for each data set and used to normalize the experimental spectra for VSF power. Daily calibration of the tunable IR beam was performed by measuring the absorption of a polystyrene standard and fitting to the known assignments. Spectra presented here are averages of ∼6 or more spectra taken over multiple days. The resolution of the VSF system used herein is ≅10 cm^{-1}.

Shallow glass dishes (≥8 mm depth) are utilized as sample cells and are cleaned according to the rigorous protocol described in previous works.[36,89,90] The dishes are placed on a vertically translatable stage. The stage is adjusted between each scan to account for any evaporation. Care was taken to ensure that evaporation did not alter the solution concentration. All VSF measurements were acquired at room temperature (∼20 °C) under ambient conditions.

2.3. Surface Tension. Contributions to the VSF signal from number density and molecular orientation are decoupled experimentally through the use of Wilhelmy plate[91] surface tensiometry measurements. The force exerted on the plate by the solution is measured using a force balance (KSV). Surface tensions (γ) are converted to surface pressures (π) by subtracting the daily measured surface tension of neat water. The platinum plate was cleaned and rinsed repeatedly in 18.2 MΩ nanopure water and then dried under flame between measurements. All measurements were recorded under ambient conditions at room temperature (∼20 °C).

It is worth noting that the surface tension versus time measurements reveal an extremely slow adsorption of HA to the interface. Equilibrium values occur after >5 h with a slowed

DOI: 10.1021/acs.jpca.8b01193
J. Phys. Chem. A 2018, 122, 3837−3849

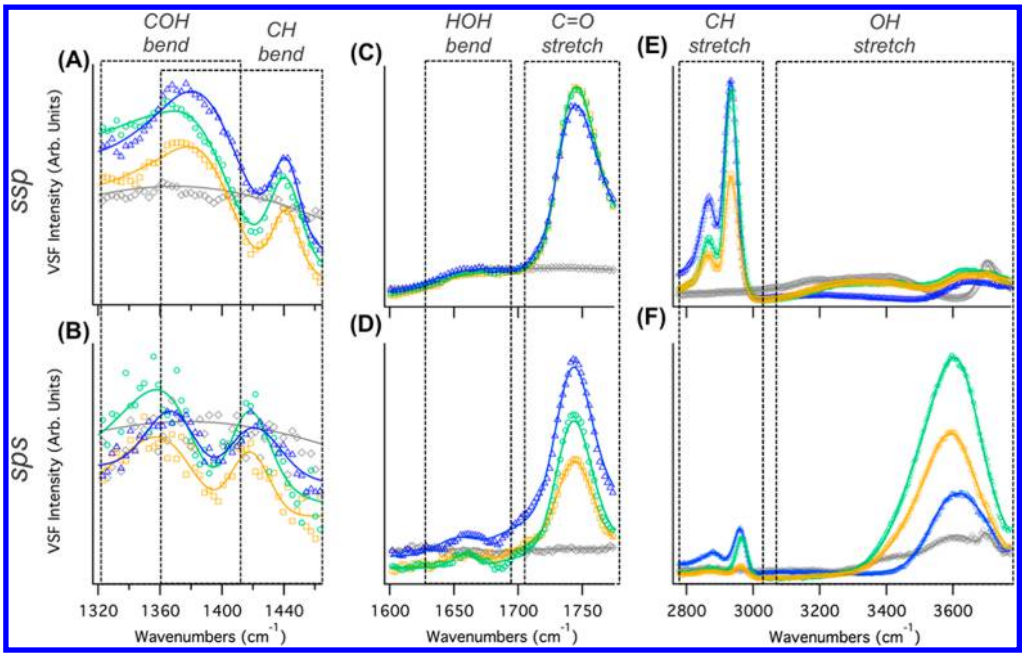

Figure 1. VSF experimental data (open circles) and corresponding fits (solid lines) for water and aqueous HA solutions in the COH/CH bending region (A, B), C═O stretching region (C, D), and the CH/OH stretching region (E, F) in the *ssp* polarization (top) and *sps* polarization (bottom). Water (gray, diamonds), 0.25 M HA (orange, squares), 0.5 M HA (green, circles), and 2 M HA (dark blue, triangles). Dotted boxes are for visual reference of approximate spectral regions.

increase over the next 24 h. This slow equilibration time is not unexpected as it has been observed in similar systems such as aqueous methylglyoxal.[36,39] Further note that VSF itself is an extremely sensitive probe of interfacial contaminants and that no evidence of contamination was observed. For this reason, VSF spectra were obtained after each sample had equilibrated (for at least 2 h) confirmed by the invariance of VSF results over time.

2.4. Sample Preparation. Aqueous HA solutions (0.1−5 M) were prepared volumetrically by diluting HA stock solution (90 wt % in H_2O, Sigma-Aldrich) in nanopure (18.2 MΩ) water. Since HA is extremely hydroscopic, the impurities contributing to the other 10% are attributed to solvated water.[62,63,65] Solutions were prepared ≥24 h before use and stored in Pyrex flasks.

2.5. Computational Methods. A combination of computational techniques is used to generate calculated VSF spectra. In addition to simulating spectra, the analysis also extracts structural details about the system, such as density profiles, as well as depth-resolved orientation and conformation information, which are vital in helping to understand the behavior of the system. This methodology is ideal because it is both computational efficient for the systems of interest and highly adaptable. This approach has been shown to be robust for numerous and varied chemical systems when compared with experimental spectra.[36,89−97]

2.5.1. Classical Molecular Dynamics. Classical molecular dynamics (MD) simulations were performed using the Amber 12 suite of programs,[98] using parameters and force fields derived in the same manner as in previous studies.[92,93] PACKMOL[99] was used to create starting configurations. In each simulation, a specific number of HA and water molecules were arranged to form a 30 Å cube within a 30 Å × 120 Å × 30 Å simulation box, with periodic boundary conditions, forming a water slab with two surfaces. To preserve the volume of the system within the larger simulation box, as the number of HA molecules increased the number of water molecules was decreased, maintaining a total of ∼2700 atoms. Simulations were performed for configurations of 1, 2, 4, 8, 16, 32, 80, and 160 HA molecules, corresponding to concentrations of ∼0.05, 0.1, 0.25, 0.5, 1, 2, 5, and 10 M HA, respectively. In each configuration, the system was energy minimized at 0 K and equilibrated (by evolution through 2 ns of simulation from 0 to 298 K), before being further evolved at 298 K in 1 fs time steps for a total of 50 ns, according to the methodology outlined in previous studies.[92,93]

2.5.2. Quantum Mechanical Calculations. Density functional theory (DFT) calculations are performed using the B3LYP exchange-correlation functional and a 6-311++G-(2d,2p) basis set within the Gaussian 09[100] program package. Geometry optimizations, dihedral potential energy scans, and harmonic vibrational frequency calculations, as well as polarizabilities and dipole moments at displaced geometries along each normal mode, are performed for all reasonable gas phase conformers. Second-order vibrational perturbation theory is used to calculate anharmonic corrections to vibrational frequencies. Specifics of the resulting DFT structures are provided in the Supporting Information.

Generating VSF spectra requires the second-order susceptibility tensor for all major conformations and orientations sampled in a dynamical interfacial system. Thus, for each normal mode of each HA conformer, the polarizabilities and dipole moment derivatives were calculated using three-point finite differentiation and combined according to eq 2 to approximate the second-order linear susceptibility response tensor.

$$\chi^{(2)}_{ijk} \propto \sum_{a,b,c} C_{abc} \frac{\partial \alpha_{ab}}{\partial Q_q} \frac{\partial \mu_c}{\partial Q_q} \tag{2}$$

Here, α is the molecular polarizability, μ is the dipole moment, Q_q is the normal coordinate of the mode q, and C is a

DOI: 10.1021/acs.jpca.8b01193
J. Phys. Chem. A 2018, 122, 3837−3849

geometrical factor relating the molecular and laboratory reference frames.

Using an in-house code,[97] VSF intensities and phases were then calculated by inspecting the second-order susceptibility tensor and assigning the static gas phase DFT structures with the molecular orientations and conformations populated in the MD simulations. The calculated intensities were empirically broadened using Lorentzian and Gaussian widths informed by the experimental VSF spectral fits.

3. RESULTS AND DISCUSSION

3.1. Experimental VSF Spectra. VSF spectra were acquired for neat water and a series of HA concentrations (0.1, 0.25, 0.50, 1, and 2 M) in the *ssp* and *sps* polarizations for the COH/CH bending, C═O stretching, and CH/OH stretching regions. For clarity, a subset of these solutions (0.25, 0.5, and 2 M, along with neat water) is shown in Figure 1. Spectra of the full concentration series are provided in the Supporting Information, along with a description of the neat water VSF spectra. The strong VSF response in each spectral region confirms that HA has a high degree of surface activity and is oriented at the interface. As shown in Figure 1, features associated with CH and C═O modes grow in above the neat water spectra with increasing HA concentration, [HA]. The spectra shown in Figure 1 also contain contributions from oriented water at the interface, complicating their interpretation. Spectra of HA in D_2O were acquired in the COH/CH bending and C═O stretching regions (Figure 2) to help isolate and confirm the assignment of water and COH modes.

Overall, there is a transition point in the spectral trends of all three regions around 0.5 M HA, where intensity associated with CH modes generally continues to increase while intensity associated with OH and COH modes decreases and/or shifts in frequency. The COH/CH bending region (Figure 1A,B) contains two broad features at ∼1370 cm^{-1} (coupled COH and CH deformations) and 1420 cm^{-1} (CH deformations) that increase in intensity with [HA] until 0.5 M. At higher [HA], the 1420 cm^{-1} feature increases in the *ssp* spectra but decreases in the *sps* polarization scheme. Within each polarization, the lower frequency feature shows greater variation. Since the COH bending mode contributes more to the intensity in this part of the spectra (demonstrated by the decreased intensity when solvating HA in D_2O, Figure 2A,B), these trends are consistent with a change in hydroxyl solvation environment. This is supported by spectra in the OH stretching region (Figure 1E,F), where the maximum OH intensity occurs at 0.5 M, before decreasing and slightly blue-shifting at higher [HA]. This blue-shift is likely indicative of a less-solvated OH stretching mode, but from this region alone one cannot distinguish between an HA associated OH mode and one associated with water.

In the CH stretching region (Figure 1E,F), there are two dominant bands of intensity present in both *ssp* and *sps* polarizations. These features are around ∼2900 and ∼2950 cm^{-1}, respectively. Their likely origins are discussed later in this paper. They increase in amplitude with increasing [HA] until 0.5 M. Above that concentration, the ∼2900 cm^{-1} feature continues to rise with [HA], but the ∼2950 cm^{-1} feature plateaus. In the C═O stretching region (Figure 1C,D), the carbonyl mode at ∼1745 cm^{-1} increases with [HA] above 0.5 M in the *sps* polarization, while decreasing in the *ssp* polarization.

Some of these changes can be simply explained by a loss of water from the interface with increasing HA surface coverage. Yet, it is interesting to note that water is not completely excluded above 0.5 M HA, as evidenced by the continued presence of interfacial water modes. In Figures 1C and D, in addition to the intense C═O stretching mode (∼1745 cm^{-1}), there is also a low-intensity feature centered around ∼1650 cm^{-1}, which is attributed the bending mode of water.[69,101−103] This assignment is confirmed by the loss of the feature when solvating HA in D_2O (Figure 2A,B). The persistence of some interfacial water at higher [HA] is not unexpected given the well-known hygroscopicity of HA.[62,63,65]

This interfacial water can have significant spectral implications, as shown by further analysis of the C═O stretching mode (Figure 2C,D). Initial fitting of the main feature to a single carbonyl mode yielded peak positions of ∼1742 and ∼1752 cm^{-1} for the *ssp* and *sps* polarizations, respectively. These assignments are somewhat implausible, since they are higher frequencies than any of the gas-phase IR or Raman literature assignments.[62,63,65] However, allowing a second feature of opposite phase resulted in more plausible frequency positions at ∼1725 cm^{-1} (negative phase, more H-bonded) and ∼1737 cm^{-1} (positive phase, less H-bonded). These fits also suggest that the apparent frequency shift between polarization schemes is due to differing relative intensities of the two C═O stretching modes. If correct, such fits imply the existence of either carbonyl moieties in more than one solvation environment and/or more than one conformation. To investigate this further, computational studies were pursued (discussed further below).

However, variations in water content, alone, cannot explain why spectral features arising from relatively solvation-insensitive CH stretching and bending modes do not increase concomitantly with increasing [HA]. The complexity of the system is further highlighted by attempts to fit the two main

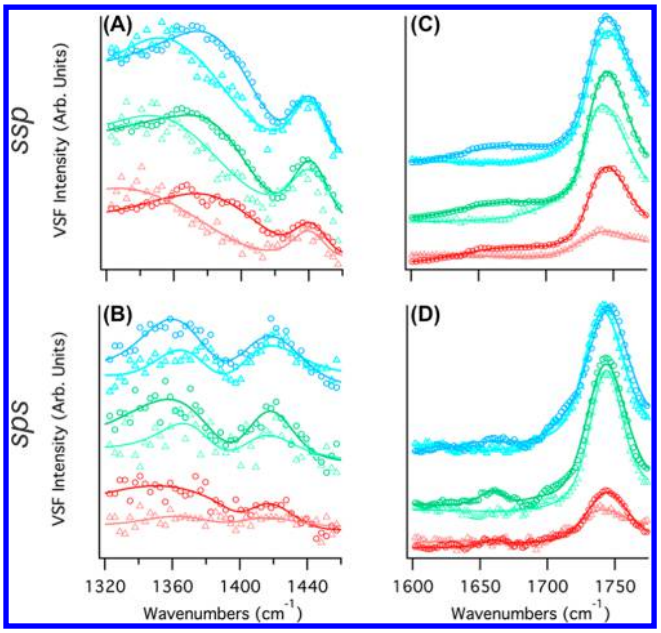

Figure 2. VSF experimental spectra for HA in H_2O (open circles) and D_2O (open triangles) and corresponding fits (solid lines) in the COH/CH (A, B) bending and C═O stretching (C, D) regions in the *ssp* (top) and *sps* (bottom) polarization schemes for 0.1 M HA (red), 0.5 M HA (green), and 1 M HA (blue). Spectra are vertically offset for clarity.

DOI: 10.1021/acs.jpca.8b01193
J. Phys. Chem. A 2018, 122, 3837−3849

features in the CH stretching region, which are shown in greater detail in Figure 3. Comparing the VSF spectra of the same [HA] in each polarization scheme reveals a shift in peak position of both features. Following the typical fitting protocol of using the minimum number of peaks, it is possible to fit these features to only two modes, but the fit does not converge to the same frequency positions between polarizations and yields implausibly high Gaussian broadenings. In fact, the full width at half-maximum (fwhm) of these features is >45 cm^{-1}, significantly higher than would be expected from singular a CH stretching mode, which are generally more on the order of ∼10 cm^{-1}.[80] The shift in peak position, combined with the broad fwhm, signifies spectral congestion arising from the overlap of multiple CH stretching modes and/or environments that contribute to each of the two observed features.

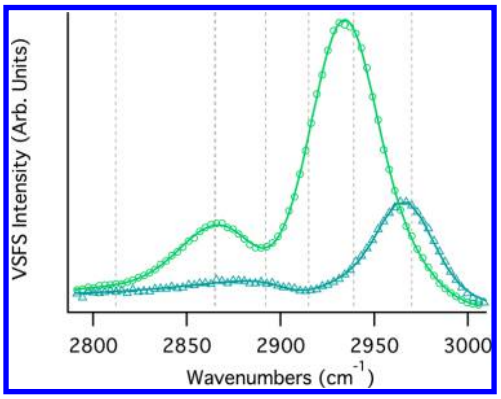

Figure 3. Experimental *ssp* (green, circles) and *sps* (teal, diamonds) VSF CH stretching data and corresponding fits (solid lines) for 0.5 M HA. The dotted gray lines denote the position of HA peaks.

The spectral congestion in this region could potentially be due to the presence of more than one HA conformer at the interface, and as previously mentioned, additional HA conformers could also explain the pair of carbonyl modes found in the C═O stretching region. The conformational distribution of HA has been the focus of many of the spectroscopic studies on HA to date.[59,61−63,65−67] Briefly, the primary form of HA in the gas phase is the closed form *cis* conformation (*Cc*), which forms a five-membered ring stabilized by an intramolecular hydrogen bond. Compared to the open form *trans* configuration (Tt), the gas phase *Cc*:Tt ratio was calculated to be 99:1.[66] However, condensed phase experiments have indicated additional conformers might be present in the aqueous solutions, specifically open form species that facilitate intermolecular hydrogen bonding and aggregation.[59,62,63,65] Computational studies by Sharma et al. calculated populations of open form *cis* and *trans* configurations (Ct and Tt, respectively) in the solution phase to be in a *Cc*:Tt:Ct ratio of 83:11:6.[65] Sharma et al.[67] also found that upon crystallization into the solid phase HA takes on the Ct form, which was later confirmed by the work of Lasne et al.[61] Low-temperature studies also discovered that in this open configuration HA can form H-bonded dimers and trimers via dual intermolecular hydrogen bonds with both the carbonyl and hydroxyl oxygen of other HA molecules.[67] This implies the potential for multiple solvation environments per conformer.

Examining each vibrational mode in both polarization schemes and D_2O uncovered some of the complexities of HA at the air−water interface—in particular, the systematic shift in the spectral behavior above 0.5 M HA and the presence of multiple HA conformations. Nonetheless, uncertainty in the assignments of the underlying modes precludes using the experimental fits for further spectral analysis without more information. To address outstanding concerns about the interfacial conformations and orientations of HA, complementary experimental and computational techniques are employed. The information gained from these techniques provides the context necessary to understand the interfacial trends giving rise to the experimental VSF spectra.

3.2. Depth Dependent Behavior. *3.2.1. Experimental Surface Tensiometry.* Equilibrium surface pressure data for aqueous solutions (0.1−5 M) are plotted in Figure 4A. The surface pressure data follow a Langmuir isotherm indicating adsorption of HA at the air−water interface: at lower [HA], the surface pressure increases linearly until ∼0.5 M, when it begins to plateau at ∼21 mN m^{-1} as the maximum surface excess is approached. Surface pressure values reported here are similar to the ∼22 mN m^{-1} value observed for methylglyoxal,[36] whose

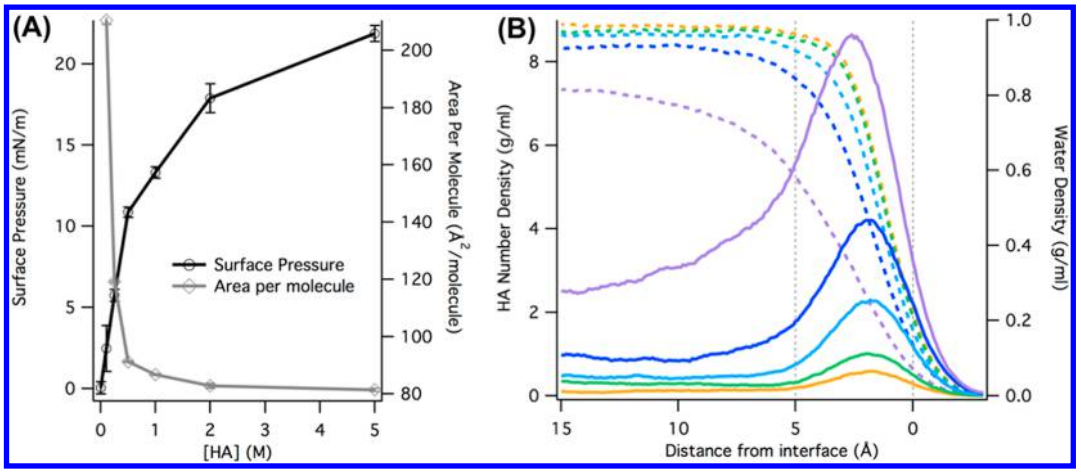

Figure 4. (A) Hydroxyacetone surface pressure (left axis, black) and surface area per molecule (right axis, gray) as a function of bulk HA concentration, [HA]. Each point represents the average of 3−7 individual samples, and the vertical error bars represent the standard deviation. (B) Density profiles of water (dotted lines) and HA (solid lines) obtained from the HA simulations with 4 HA (∼0.25 M, orange), 8 HA (∼0.5 M, green), 16 HA (∼1 M, blue), 32 HA (∼1 M, dark blue), and 80 HA(∼5 M, purple). The dotted gray lines denote the approximate boundary between the surface (0 Å) and subsurface (5 Å).

DOI: 10.1021/acs.jpca.8b01193
J. Phys. Chem. A 2018, 122, 3837−3849

dominant diol form has a structure quite similar to HA. Maximum surface excess was calculated from the surface pressure data according to the Gibbs adsorption equation, as previously described.[36,90,104] An estimate for the minimum average area per molecule of HA was found to be ~80 Å^2 mol^{-1} (again, comparable to the 73 Å^2 per molecule calculated for methylglyoxal). For a molecule the size of HA, this corresponds to moderate to low surface packing. Thus, the surface pressure data support the main VSF findings of (a) HA populating the air−water interface and (b) water at the interface, even at the highest [HA] loadings. However, surface tensiometry cannot provide insight into the identity and orientation of HA conformers at the surface.

3.2.2. Computational Results: Density Profiles and Conformer Distributions. Despite the exquisite surface sensitivity of VSF and the assistance of surface tensiometry, aspects of HA's surface behavior still remain undetermined. In order to further deconvolve the contributions of surface population and orientation that give rise to the experimental VSF spectra, MD simulations of HA were analyzed to determine the depth dependent behavior of HA.

The density profiles of HA and water obtained from each simulation are shown in Figure 4B. Since the amount of water in each simulation was scaled to preserve the volume of the box, the location of the interface is defined as being where the density of HA is at 50% of its peak value. This point was found to be within ±1 Å for all HA simulations and defined as 0 Å. In each simulation, HA shows an affinity for the interface and increasing surface coverage with [HA]. This agrees with the experimental surface tensiometry results and adds an additional level of detail. A subsurface enhancement begins at ~5 Å and peaks at ~2 Å. At first glance, the HA interface appears to precede the water interface with increasing [HA], signifying some degree of water exclusion and increased HA surface coverage at the interface. However, the water profile actually becomes more gradual, indicating a broader boundary where the water is solvating an amorphous HA layer rather than forming a delineated interface with HA.

To appreciate what implications this has for the VSF results, the depth dependence of HA's condensed phase conformational space was examined. Calculated DFT structures for HA are shown in Figure 5A. Four gas phase minima were found by examining the dihedral potential energy surface. These are in agreement with previous findings in the literature.[65]

As previously mentioned, the conformational population distributions of HA have been a subject of much interest.[59,61−63,65−67] To briefly expand on this, the HA1-*Cc* conformer is the dominant structure in the gas phase, with only minimal contributions from any *trans* configuration.[62,65] Mohačék-Grošev analyzed HA in the solution phase and assigned the contributions to a general *cis* conformer but noted the presence of unassigned modes that were likely due to a *trans* configuration.[63] Later simulations by Sharma et al.[65] established that a *cis* conformer with a *gauche* hydroxyl group was the most abundant conformer in the solution phase—though not favorable in the gas phase. In this work, the MD simulations also yielded this additional structure, denoted HA5-Cg, which accounts for ~50% of bulk HA. The favorability of HA5-Cg in the solution phase is because the gauche orientation of hydroxyl group allows for greater intermolecular hydrogen bonding. Experimental support of this is provided by Jetzki et al.,[59] whose work proposes that the gas and particle phase HA spectra might have differing dominant conformers. The authors

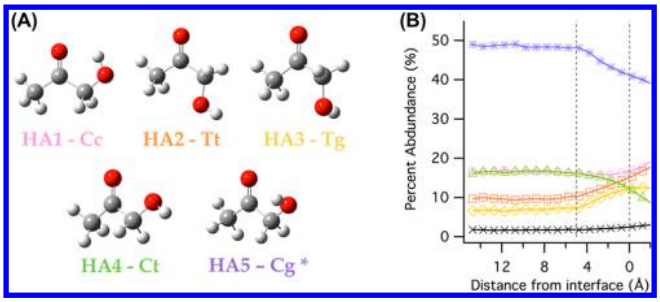

Figure 5. (A) Gas phase DFT structures of HA at the B3LYP/6-311++G(2d,2p) level of theory (*not a minimum on the gas phase potential energy surface). (B) Percent abundance of the HA conformers as a function of depth from the interface (16 HA molecules, ~1 M). HA1-*Cc* (red, circles), HA2-Tt (orange, squares), HA3-Tg (green, diamonds), HA4-Ct (blue, triangles), HA5-Cg (purple, stars), and unassigned conformations (X's). The dotted gray lines denote the approximate boundary between the surface (0 Å) and subsurface (5 Å).

posited the existence of HA5-Cg in the condensed phase, arguing that the freedom to take part in intermolecular hydrogen bonding and the formation of aggregates might supersede the favorability of the intermolecular hydrogen bond of HA1-*Cc*.

The MD simulations support the presence of multiple conformers at the interface. Figure 5B illustrates how the relative abundance of the five conformers varies as a function of depth from the interface. Little change was observed at different simulation concentrations, so only the results for the HA 16 (~1 M) simulation are presented. Note that while HA5-Cg is the most abundant conformer for both the bulk and interface, its relative abundance decreases slightly near the interface (as does HA4-Ct, to a lesser extent). This is consistent with HA5-Cg not being a stable gas phase conformer and with HA4-Ct being the least energetically favorable in gas phase. At ~5 Å these two conformers decline in abundance, while the two *trans* conformers, HA2-Tt and HA3-Tg, begin to increase. This is the same depth at which the subsurface enhancement was observed in the density profiles (Figure 4B), supporting that this change in preference is surface mediated. Intriguingly, HA5-Cg is still the dominant conformer at the interface (accounting for ~40%); the relative abundance of the remaining conformers tracks more closely to their gas phase hierarchy (with HA1-*Cc*, the dominant gas phase conformer, leading at ~20%). The ratio between the most abundant *cis* and *trans* conformers (HA5-Cg and HA2-Tt, respectively) is higher in the bulk (~5:1) than at the interface (~3:1), further emphasizing the behavior changes at the interface.

The depth dependent orientation of HA was analyzed in each simulation to determine average distributions of specific bond angles (with respect to the surface normal) within each 1 Å slice of the box (Figure 6). It is important to emphasize that the aqueous HA interface is highly dynamic and that these are very much statistical averages. As such, the peak of the distribution signifies a preference to tend toward that orientation, but as evidenced by the broadness of the distributions, the molecules are also continually moving and reorienting. Examination of the angle distributions for the individual HA conformers reveals orientations that are both depth and conformer dependent.

Figure 6 shows percent abundance per conformer for the C−CH_3 (A, B), methylene CH (C, D), and C═O (E, F) bond

DOI: 10.1021/acs.jpca.8b01193
J. Phys. Chem. A 2018, 122, 3837−3849

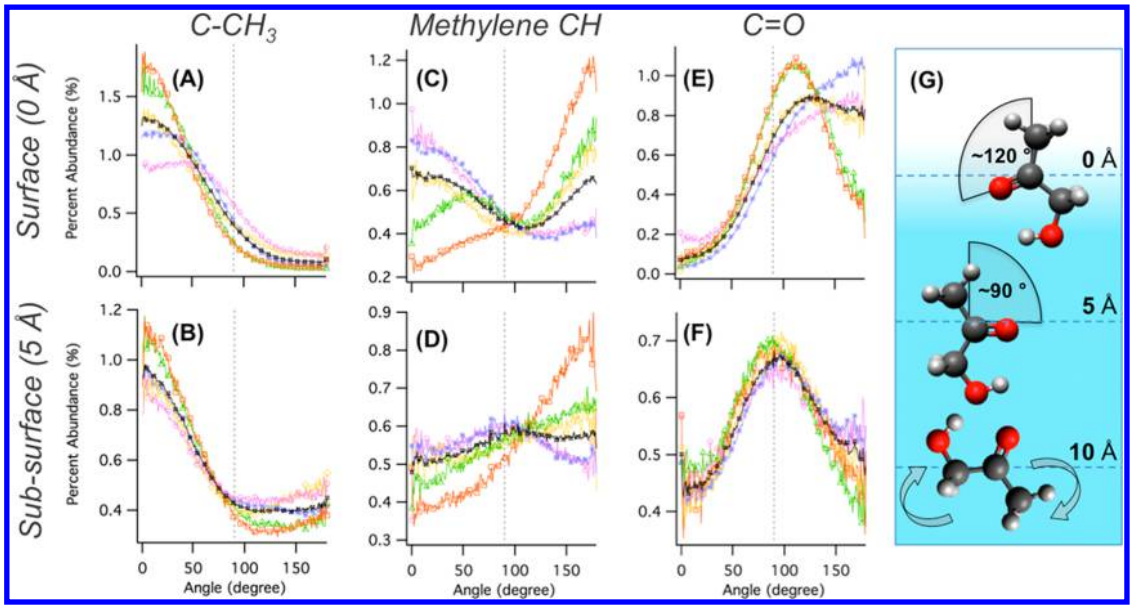

Figure 6. Normalized distributions of HA bond angles (relative to the surface normal into the vapor phase) for a simulation with 80 HA molecules (~5 M). Percent abundance for the total HA system (black, open ×'s) and individual HA conformers (HA1-*Cc* (pink, circles), HA2-Tt (orange, squares), HA3-Tg (gold, diamonds), HA4-Ct (olive, triangles), HA5-Cg (purple, stars)) are displayed for the C−CH_3 (A, B), methylene CH (C, D), and C═O (E, F) bond angles at the surface (0 Å, top) and subsurface (5 Å, bottom), respectively. (G) Visual representation of the C═O bond angle orientation as a function of depth from the interface. In the bulk (~10 Å), the orientation is isotropic and HA has no average net orientation (indicated by the curved arrows).

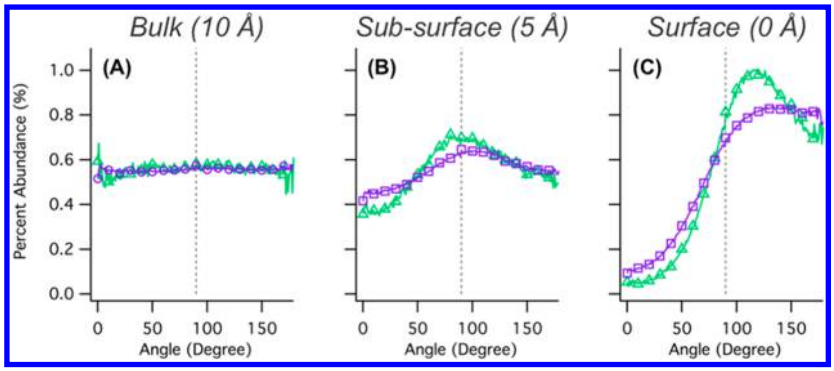

Figure 7. Concentration dependence in the C═O bond angle orientation for (A) the bulk (10 Å), (B) the subsurface (5 Å), and (C) the surface (0 Å, bottom), for simulations with 8 HA (~0.5 M) (green) and 80 HA (~5 M) (purple).

angles at the subsurface and surface. In each plot, the black lines represent the percent distribution across all conformers while the colored lines correspond to angle distributions for individual conformers. Figure 6G provides a graphic representation of the overall C═O bond angle orientation as a function of depth (black lines in Figure 6E,F). The C═O bond angle shifts from ~90° at the subsurface (~5 Å deep) to ~120° at the surface (~0 Å deep). However, the individual conformations reveal additional variation for a given depth.

With the C═O bond angle, the conformers all have a similar orientation in the subsurface region centered at ~90° (Figure 6F). But at the surface (Figure 6E), the HA2-Tt and HA4-Ct species both show a well-defined peak at ~120° while the other three conformers have shifted into a broader peak, centered closer to ~180°. The methylene CH bond angles show a similar trend. At ~5 Å deep (Figure 6D), the HA2-Tt conformer and, to a lesser extent, HA3-Tg and HA4-Ct tend to have methylene CH bonds pointed toward the vapor phase while the HA1-*Cc* and HA5-Cg show a minute enhancement parallel to the interface at ~90°. At the interface (Figure 6C) again the HA2-Tt conformer shows little change, but HA1-*Cc* and HA5-Cg strongly reorient toward ~0° (where methylene CH bonds would be pointed out of the interface) while HA3-Tg and HA4-Ct take on a bimodal distribution, with preferences for orientation at ~45° and ~180° (one methylene CH bond pointed into the vapor phase with the other pointed into the condensed phase). The orientation of the methyl group is more consistent between the subsurface and surface (Figures 6A and 6B, respectively), with a strong preference to point into the vapor phase. But the HA1-*Cc* distribution (and to lesser degree HA5-Cg) broadens somewhat, peaking closer to ~45°, indicating a more variable orientation.

From Figure 6, it is evident that the broadened angle distributions observed in the total system (black lines) cannot be viewed in the context of a uniform change in orientation. The individual conformer orientations are far more complicated, in support of the VSF spectra, which suggest multiple conformers in different orientations. It is worth noting that the HA4-Ct conformer tracks more closely with the HA2-Tt conformer than with the other two *cis* conformers, whereas the

DOI: 10.1021/acs.jpca.8b01193
J. Phys. Chem. A 2018, 122, 3837−3849

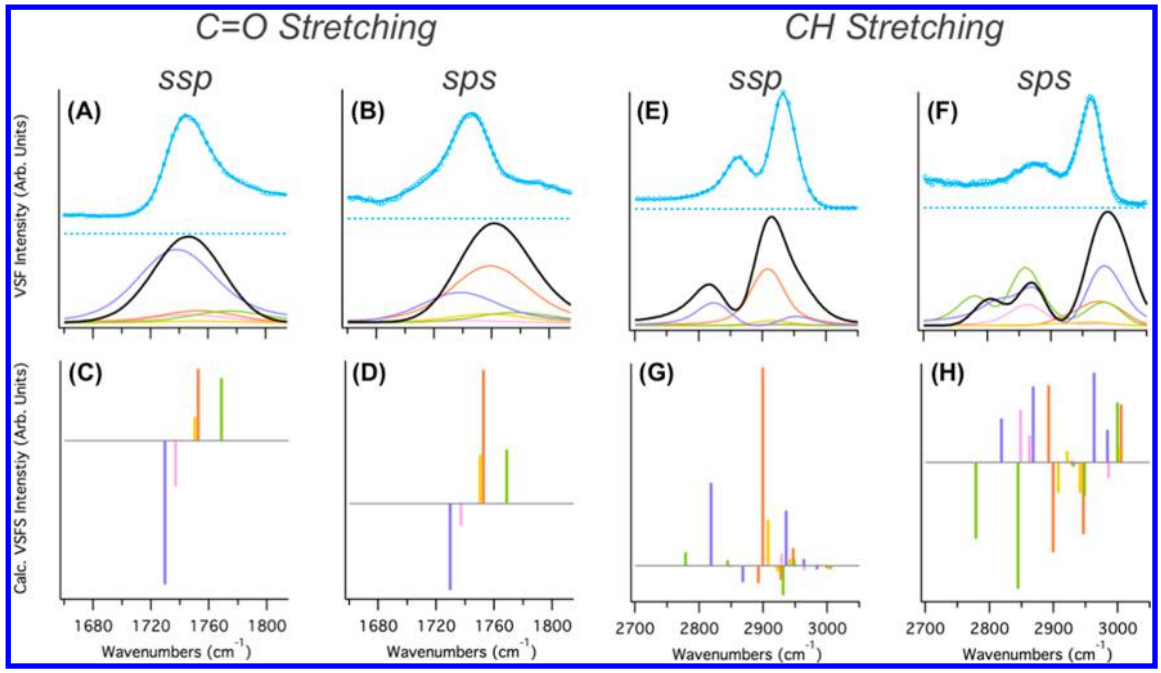

Figure 8. Experimental VSFS vs calculated VSF spectra from the 16 HA (∼1 M) simulation in the CO stretching (A−D) and CH stretching (E−H) regions. Top: *ssp* (A, E) and *sps* (B, F) polarized experimental VSF of 1 M HA spectra (offset, blue, data = circles, fit = line) and the calculated VSF spectra for the total spectrum with all HA conformers (black) and the individual conformer contributions of HA1-*Cc* (pink), HA2-Tt (orange), HA3-Tg (gold), HA4-Ct (olive), and HA5-Cg (purple) stretching region compared to the calculated spectra of the full 16 HA (∼1 M). Bottom: calculated intensities and phases in the *ssp* (C, G) and *sps* (D, H) polarization for the HA conformers (positive and negative intensities represent phases of 0 and π, respectively).

HA3-Tt conformer tends to fall somewhere between the others. This indicates that the C−C−O−H dihedral (lower case letter) has a larger role in the interfacial orientation of HA than the O═C−C−O dihedral (capital letter). Since external hydrogen bonding is the factor most likely to involve the orientation of the OH group, this arrangement signifies a tendency for HA to form ordered hydrogen-bonded aggregates at the interface, as has been proposed in the literature.[59,62,65]

Intuitively, one might expect this tendency to aggregate to be amplified with increasing [HA]: as HA further populates the interface, more water is in turn excluded and other HA molecules become more abundant for aggregation. This increased HA population also creates additional favorable ways for HA orient itself, as indicated in Figure 7 by the broadening of the angle distributions at higher [HA]. This could explain some of changes in intensity with [HA] observed in the experimental VSF spectra.

3.3. Application of Computational Results with Spectral Interpretations. The results discussed in the previous section provide a deeper understanding of the depth, concentration, and conformation dependent population and orientation dynamics of HA. Here the experimental VSF spectra can be reconsidered in context of these findings and agreement with calculated VSF spectra. Assessment of calculated VSF spectra enable further analysis by decoupling the spectral contributions arising from each HA conformer and providing insight into how these contributions convolve together to produce the overall spectrum. It is important to note that the current implementation of the methodology does not include contributions to the experimental intensity arising from water. Additionally, only contributions from fundamental vibrations are calculated, so intensity from any Fermi resonance, overtone, or combination band is excluded. Barring these limitations, the calculated spectra are able to reproduce the experimental VSF data for spectral regions arising from fundamental modes that are insensitive to solvation as previously demonstrated.[36,89,90,92,97]

Figure 8 shows both experimental and calculated 1 M HA spectra in two different vibrational regions (CO stretching and CH stretching) and for both polarizations schemes (*ssp* and *sps*). The blue (topmost) traces in parts A, B, E, and F are the experimental results for 1 M HA in H_2O. Directly beneath each of these are the spectral contributions calculated for each of the five individual HA conformers (colored traces) plus the calculated total spectrum (black). In both polarizations and for each region, the calculated spectra are a good overall match to experiment.

The intensity and phase of the modes giving rise to these calculated spectra are displayed in the bottom of Figure 8C,D,G,H. These intermediate results (referred to as "stick spectra") are the initial outputs of the VSF calculation routine, which are broadened according to eq 2 to generate the calculated spectra. The stick spectra provide a guide to the phases and intensities of these modes that explains the resulting destructive or constructive interference in the resulting total VSF spectrum.

A few specifics immediately stand out in these calculated spectra. In general, the HA5-Cg (purple) and HA3-Tt (orange) conformers contribute the most in the calculated VSF spectra, which agrees with the previous literature predictions regarding the dominant condensed phase species.[65] It is not surprising that HA5-Cg has a dominant conformation since it was revealed by the MD simulations to be the most abundant conformer at the interface. (For clarity, only these two most abundant conformers will be discussed here.) The phase information revealed by the stick spectra provides significant

DOI: 10.1021/acs.jpca.8b01193
J. Phys. Chem. A 2018, 122, 3837−3849

Table 1. Frequencies and Assignments of Peaks from Experimental *ssp* and *sps* Polarized VSF Spectra

mode no. ν_i	*ssp* exptl freq (cm^{-1})[a]		*sps* exptl freq (cm^{-1})[a]		bulk IR (cm^{-1})[62]	gas phase IR (cm^{-1})[62]	assignt (mode)[b]
ν_{12}	1363	π			1359	1356.56	sym-δCH_3 sym, CH_2 wag + νCCC AS
ν_{11}			1380	π	1378	1411.35	CH_3 scissors + δCOH
ν_{10}	1405	0	1405	0	1405	1446.53	CH_2 δHCO/CH_2 wag + δCOH
ν_9	1420	0	1420	0	1418	1448.69	δCH_3 AS′ + CH_2 scissors
ν_8	1442	0	1442	π	1438	1469	δCH_3 AS″/CH_2 scissors
ν_7	1725	π	1725	π	1724		C═O stretch (more H-bonded)
$\nu_{7'}$	1737	0	1739	0		1741.49	C═O stretch (less H-bonded)
$2\nu_{10}$	2808	0			2810	2803	overtone ($2\nu_{10}$)
ν_6	2855	0			2842	2862	νCH_2 SS (*cis*-HA)
ν_5	2902	π	2907	0	2897	2885	νCH_2 SS (*trans*-HA), νCH_2 AS (*cis*-HA)
ν_4	2915	0	2912	π	2921	2917	νCH_2 AS (*trans*-HA)
ν_3			2954	π	2939	2973	νCH_3 AS, νCH_3 SS (*trans*-HA)
ν_2		0	2966	0	2989	3022	νCH_3 AS
$\nu_{1'}$	~3250	0	~3550	0	3417		νOH (H-bonded)
ν_1	3604	0	3610	0		3523.68	νOH (HA)

[a]Experimental fit frequencies ± 10 cm^{-1}. [b]δ = bend; ν = stretching; AS′ = (in-plane); AS″ = (out-of-plane), "+" = "and"; "/" = "or".

new insights into how these conformers combine to produce the resulting line shape.

In the C═O stretching region, the underlying stick spectra (Figure 8C,D) display the frequency and phase of the C═O mode for each conformer. In both polarizations, the HA5-Cg (and HA1-*Cc*) is lower in frequency with a negative phase while HA2-Tt (and the other two conformers) is at a higher frequency with a positive phase. Additionally, HA5-Cg has the greatest relative intensity in the *ssp* spectrum, while HA2-Tt is the most intense in the *sps* spectrum. Recall that the experimental C═O spectra were fit to two peaks with opposite phase: a negative peak at ~1725 cm^{-1} (attributed to a more strongly H-bonded carbonyl) and a positive peak at ~1737 cm^{-1} (attributed to a less strongly H-bonded carbonyl). This agreement between the calculated spectra and experimental fits provides significant evidence of more than one species of carbonyl at the interface. Because of the lack of solvation effects included in our methodology, this alone cannot differentiate if the agreement is due to the conformation or solvation environment, but it does clearly indicate that the experimental C═O is in a continuum of hydrogen bonding environments at the interface.

In the CH stretching region (Figure 8E–H), HA5-Cg and HA2-Tt also have significant contributions in both polarizations. In fact, HA5-Cg and HA2-Tt are the main sources of intensity in the *ssp* polarization calculated VSF spectra (Figure 8E), and the stick spectra (Figure 8G) show that the most intense peak arises from HA2-Tt at ~2900 cm^{-1} (CH_2 symmetric stretch). Once broadened, this positive phase peak interferes constructively with the positive HA5-Cg peak at ~2935 cm^{-1} (CH_3 symmetric stretch). Thus, both methylene and methyl modes contribute to the single tall, broad peak to the high-frequency side of the total spectrum. The remaining feature at ~2850 cm^{-1} largely arises from CH_2 symmetric stretching modes (positive phase) of HA5-Cg.

The CH stretching region is more complicated in the *sps* polarization (Figure 8F) due to larger contributions from the other conformers as well. Surprisingly, the low-frequency side of the HA4-Ct spectrum (Figure 8F, green) is slightly more intense than HA5-Cg, but the total calculated spectrum (Figure 8F, black) does not reflect this additional intensity. The stick spectra in Figure 8H reveal that these HA4-Ct modes are out of phase with those of the other two *cis* conformers, bringing down the intensity of the total VSF feature there. On the high-frequency side of the CH region (~3000 cm^{-1}), the intensity arises from the positive phases of CH_3 asymmetric stretching modes of all five conformers interfering constructively. These two clusters of positive phase modes on either side of the spectrum border an intense cluster of negative phase peaks between ~2900 and 2950 cm^{-1}. These negative phases in the stick spectra are due to the CH_2 and CH_3 symmetric stretches of the two *trans* conformers as well as the methyl asymmetric stretch of HA4-Ct. These negative phase modes line up extremely well with the sharp dip seen in the experimental spectrum.

Overall, the agreement between the calculated and experimental spectra indicates that both the open form *cis* and *trans* conformers of HA are present at the air–water interface. With the phase information provided by the stick spectra, the experimental spectra can be examined in context of the underlying conformational contributions. The resulting experimental VSF spectral assignments are displayed in Table 1.

4. CONCLUSIONS AND ATMOSPHERIC IMPLICATIONS

Calculated and experimental VSF spectra have been presented and demonstrate that HA (a small organic molecule and not a traditional surfactant) demonstrates a substantial surface activity. HA is oriented at the air–water interface but also highly dynamic in regards to conformation, concentration, and depth dependent behavior. The system transitions from a diffusion limited regime into a surface excess limited regime around 0.5 M HA. The relatively large surface area per molecule and calculated density profile support the presence of solvated water in a surface layer that is largely HA. The continued presence of water is evidenced in experimental VSF spectra by the loss of key spectral features when solvating HA in D_2O. The contributions of water modes to the VSF spectra demonstrates that the interfacial water is coordinating in an ordered way, even at the highest HA concentrations.

The VSF spectra also show evidence of either multiple HA conformers or solvation environments at the interface. Analysis of MD simulations shows that the open *cis* form of HA (with the hydroxyl H at a *gauche* offset to the carbonyl) is the most abundant conformer in the bulk (~50%) and at the interface

DOI: 10.1021/acs.jpca.8b01193
J. Phys. Chem. A 2018, 122, 3837–3849

(~40%). The lack of an internal H-bond in the open form signifies the formation of H-bonded aggregates throughout the system. This *cis* conformer and the open form *trans* conformer (with the hydroxyl H fully *trans* to the carbonyl) contribute most strongly to the calculated VSF spectra. These two conformers exhibit differing orientations as well as depth dependent reorientations between the subsurface and surface. Interestingly, the position of the hydroxyl group was shown to have a greater effect on interfacial orientation than the *cis* or *trans* configuration. This suggests that the resulting orientation of HA may be dependent on its aggregation interactions. The ratio of open form *cis* to *trans* conformers is lower at the interface (~3:1) than in the bulk (~5:1). Since the *trans* conformer is not populated in the gas phase, this may be a sign of stabilizing interactions unique to the interface.

Together, these results create a picture of a coordinated interface composed of HA forming dynamic external hydrogen bonds with other HA and water. Furthermore, they suggest that there may be one or more preferred aggregation structures at the interface. In the future, aggregation structures could potentially be investigated by incorporating explicit microsolvation into the computational methodology and examining HA H-bonded dimer and trimer systems. This would also serve to further isolate spectral features arising from the external solvation environment from internal conformational dependencies.

HA's tendency to form surface specific coordinated aggregates may have significant implication for atmospheric interfaces, as it could impact surface properties, such as gas-to-particle partitioning and cloud condensation nuclei activity. Furthermore, because of the potential variability of these H-bonded aggregates, unanticipated cooperative effects may arise in systems of mixed organics. This work provides the foundation for HA as a quantified organic model system to use as a control in future studies of organic−salt or mixed organic systems at the air−water interface.

■ ASSOCIATED CONTENT

Supporting Information

The Supporting Information is available free of charge on the ACS Publications website at DOI: 10.1021/acs.jpca.8b01193.

VSF spectra for all hydroxyacetone concentrations and a brief discussion of VSF water spectra; plots of hydroxyactone surface pressure and surface excess; figure depicting the HA dihedral definitions and 1D potential energy surface; tables containing additional information (energies, dihedral angles, overall abundances) for hydroxyacetone DFT structures and calculated VSF intensity (PDF)

■ AUTHOR INFORMATION

Corresponding Author

*E-mail richmond@uoregon.edu (G.L.R.).

ORCID

Geraldine L. Richmond: 0000-0001-5682-6598

Notes

The authors declare no competing financial interest.

■ ACKNOWLEDGMENTS

This material is based upon work supported by the National Science Foundation under Grant CHE 1505891.

■ REFERENCES

(1) Kawamura, K.; Okuzawa, K.; Aggarwal, S. G.; Irie, H.; Kanaya, Y.; Wang, Z. Determination of Gaseous and Particulate Carbonyls (Glycolaldehyde, Hydroxyacetone, Glyoxal, Methylglyoxal, Nonanal and Decanal) in the Atmosphere at Mt. Tai. *Atmos. Chem. Phys.* **2013**, *13*, 5369−5380.

(2) Waxman, E. M.; Dzepina, K.; Ervens, B.; Lee-Taylor, J.; Aumont, B.; Jimenez, J. L.; Madronich, S.; Volkamer, R. Secondary Organic Aerosol Formation from Semi- and Intermediate-Volatility Organic Compounds and Glyoxal: Relevance of O/C as a Tracer for Aqueous Multiphase Chemistry. *Geophys. Res. Lett.* **2013**, *40*, 978−982.

(3) Ervens, B.; Turpin, B. J.; Weber, R. J. Secondary Organic Aerosol Formation in Cloud Droplets and Aqueous Particles (AqSOA): A Review of Laboratory, Field and Model Studies. *Atmos. Chem. Phys.* **2011**, *11*, 11069−11102.

(4) Ervens, B.; Volkamer, R. Glyoxal Processing by Aerosol Multiphase Chemistry: Towards a Kinetic Modeling Framework of Secondary Organic Aerosol Formation in Aqueous Particles. *Atmos. Chem. Phys.* **2010**, *10*, 8219−8244.

(5) Fu, T. M.; Jacob, D. J.; Wittrock, F.; Burrows, J. P.; Vrekoussis, M.; Henze, D. K. Global Budgets of Atmospheric Glyoxal and Methylglyoxal, and Implications for Formation of Secondary Organic Aerosols. *J. Geophys. Res.* **2008**, DOI: 10.1029/2007JD009505.

(6) Ervens, B.; Sorooshian, A.; Lim, Y. B.; Turpin, B. J. Key Parameters Controlling OH-Initiated Formation of Secondary Organic Aerosol in the Aqueous Phase (AqSOA). *J. Geophys. Res.-Atmos.* **2014**, *119*, 3997−4016.

(7) Galloway, M. M.; Chhabra, P. S.; Chan, A. W. H.; Surratt, J. D.; Flagan, R. C.; Seinfeld, J. H.; Keutsch, F. N. Glyoxal Uptake on Ammonium Sulphate Seed Aerosol: Reaction Products and Reversibility of Uptake under Dark and Irradiated Conditions. *Atmos. Chem. Phys.* **2009**, *9*, 3331−3345.

(8) Galloway, M. M.; Powelson, M. H.; Sedehi, N.; Wood, S. E.; Millage, K. D.; Kononenko, J. A.; Rynaski, A. D.; De Haan, D. O. Secondary Organic Aerosol Formation During Evaporation of Droplets Containing Atmospheric Aldehydes, Amines, and Ammonium Sulfate. *Environ. Sci. Technol.* **2014**, *48*, 14417−14425.

(9) Jang, M.; Czoschke, N. M.; Lee, S.; Kamens, R. M. Heterogeneous Atmospheric Aerosol Production by Acid-Catalyzed Particle-Phase Reactions. *Science* **2002**, *298*, 814−817.

(10) Odum, J. R.; Hoffmann, T.; Bowman, F.; Collins, D.; Flagan, R. C.; Seinfeld, J. H. Gas/Particle Partitioning and Secondary Organic Aerosol Yields. *Environ. Sci. Technol.* **1996**, *30*, 2580−85.

(11) Sareen, N.; Schwier, A. N.; Lathem, T. L.; Nenes, A.; McNeill, V. F. Surfactants from the Gas Phase May Promote Cloud Droplet Formation. *Proc. Natl. Acad. Sci. U. S. A.* **2013**, *110*, 2723−2728.

(12) Woo, J. L.; Kim, D. D.; Schwier, A. N.; Li, R. Z.; McNeill, V. F. Aqueous Aerosol SOA Formation: Impact on Aerosol Physical Properties. *Faraday Discuss.* **2013**, *165*, 357−367.

(13) McNeill, V. F. Aqueous Organic Chemistry in the Atmosphere: Sources and Chemical Processing of Organic Aerosols. *Environ. Sci. Technol.* **2015**, *49*, 1237−1244.

(14) Kroll, J. H.; Ng, N. L.; Murphy, S. M.; Varutbangkul, V.; Flagan, R. C.; Seinfeld, J. H. Chamber Studies of Secondary Organic Aerosol Growth by Reactive Uptake of Simple Carbonyl Compound. *J. Geophys. Res.* **2005**, DOI: 10.1029/2005JD006004.

(15) Heald, C. L.; Jacob, D. J.; Park, R. J.; Russell, L. M.; Huebert, B. J.; Seinfeld, J. H.; Liao, H.; Weber, R. J. A Large Organic Aerosol Source in the Free Troposphere Missing from Current Models. *Geophys. Res. Lett.* **2005**, *32* (18), L18809.

(16) Volkamer, R.; San Martini, F.; Molina, L.; Salcedo, D.; Jimenez, J.; Molina, M.; Martini, S. A Missing Sink for Gas-Phase Glyoxal in Mexico City: Formation of Secondary Organic Aerosol. *Geophys. Res. Lett.* **2007**, *34*, L19807.

(17) Volkamer, R.; Jimenez, J. L.; San Martini, F.; Dzepina, K.; Zhang, Q.; Salcedo, D.; Molina, L. T.; Worsnop, D. R.; Molina, M. J. Secondary Organic Aerosol Formation from Anthropogenic Air Pollution: Rapid and Higher than Expected. *Geophys. Res. Lett.* **2006**, *33*, L17811.

(18) Axson, J. L.; Takahashi, K.; De Haan, D. O.; Vaida, V. Gas-Phase Water-Mediated Equilibrium between Methylglyoxal and Its Geminal Diol. *Proc. Natl. Acad. Sci. U. S. A.* **2010**, *107*, 6687−6692.
(19) Corrigan, A. L.; Hanley, S. W.; De Haan, D. O. Uptake of Glyoxal by Organic and Inorganic Aerosol. *Environ. Sci. Technol.* **2008**, *42*, 4428−4433.
(20) De Haan, D. O.; Corrigan, A. L.; Smith, K. W.; Stroik, D. R.; Turley, J. J.; Lee, F. E.; Tolbert, M. A.; Jimenez, J. L.; Cordova, K. E.; Ferrell, G. R. Secondary Organic Aerosol-Forming Reactions of Glyoxal with Amino Acids. *Environ. Sci. Technol.* **2009**, *43*, 2818−2824.
(21) De Haan, D. O.; Corrigan, A. L.; Tolbert, M. A.; Jimenez, J. L.; Wood, S. E.; Turley, J. J. Secondary Organic Aerosol Formation by Self-Reactions of Methylglyoxal and Glyoxal in Evaporating Droplets. *Environ. Sci. Technol.* **2009**, *43*, 8184−8190.
(22) De Haan, D. O.; Hawkins, L. N.; Kononenko, J. A.; Turley, J. J.; Corrigan, A. L.; Tolbert, M. A.; Jimenez, J. L. Formation of Nitrogen-Containing Oligomers by Methylglyoxal and Amines in Simulated Evaporating Cloud Droplets. *Environ. Sci. Technol.* **2011**, *45*, 984−991.
(23) De Haan, D. O.; Tolbert, M. A.; Jimenez, J. L. Atmospheric Condensed-Phase Reactions of Glyoxal with Methylamine. *Geophys. Res. Lett.* **2009**, *36*, L11819.
(24) Hastings, W. P.; Koehler, C. A.; Bailey, E. L.; De Haan, D. O. Secondary Organic Aerosol Formation by Glyoxal Hydration and Oligomer Formation: Humidity Effects and Equilibrium Shifts During Analysis. *Environ. Sci. Technol.* **2005**, *39*, 8728−8735.
(25) Hazra, M. K.; Francisco, J. S.; Sinha, A. Hydrolysis of Glyoxal in Water-Restricted Environments: Formation of Organic Aerosol Precursors through Formic Acid Catalysis. *J. Phys. Chem. A* **2014**, *118*, 4095−4105.
(26) Johnson, C. M.; Tyrode, E.; Leygraf, C. Atmospheric Corrosion of Zinc by Organic Constituents I. The Role of the Zinc/Water and Water/Air Interfaces Studied by Infrared Reflection/Absorption Spectroscopy and Vibrational Sum Frequency Spectroscopy. *J. Electrochem. Soc.* **2006**, *153*, B113−B120.
(27) Krizner, H. E.; De Haan, D. O.; Kua, J. Thermodynamics and Kinetics of Methylglyoxal Dimer Formation: A Computational Study. *J. Phys. Chem. A* **2009**, *113*, 6994−7001.
(28) Liggio, J.; Li, S. M.; McLaren, R. Reactive Uptake of Glyoxal by Particulate Matter. *J. Geophys. Res.* **2005**, DOI: 10.1029/2004JD005113.
(29) Liggio, J.; Li, S. M.; McLaren, R. Heterogeneous Reactions of Glyoxal on Particulate Matter: Identification of Acetals and Sulfate Esters. *Environ. Sci. Technol.* **2005**, *39*, 1532−1541.
(30) Loeffler, K. W.; Koehler, C. A.; Paul, N. M.; De Haan, D. O. Oligomer Formation in Evaporating Aqueous Glyoxal and Methyl Glyoxal Solutions. *Environ. Sci. Technol.* **2006**, *40*, 6318−6323.
(31) Maron, M. K.; Takahashi, K.; Shoemaker, R. K.; Vaida, V. Hydration of Pyruvic Acid to Its Geminal-Diol, 2,2-Dihydroxypropanoic Acid, in a Water-Restricted Environment. *Chem. Phys. Lett.* **2011**, *513*, 184−190.
(32) Mucha, M.; Mielke, Z. Complexes of Atmospheric Alpha-Dicarbonyls with Water: FTIR Matrix Isolation and Theoretical Study. *J. Phys. Chem. A* **2007**, *111*, 2398−2406.
(33) Nemet, I.; Vikic-Topic, D.; Varga-Defterdarovic, L. Spectroscopic Studies of Methylglyoxal in Water and Dimethylsulfoxide. *Bioorg. Chem.* **2004**, *32*, 560−570.
(34) Plath, K. L.; Axson, J. L.; Nelson, G. C.; Takahashi, K.; Skodje, R. T.; Vaidaa, V. Gas-Phase Vibrational Spectra of Glyoxylic Acid and Its Gem Diol Monohydrate. Implications for Atmospheric Chemistry. *React. Kinet. Catal. Lett.* **2009**, *96*, 209−224.
(35) Romakkaniemi, S.; Kokkola, H.; Smith, J. N.; Prisle, N. L.; Schwier, A. N.; McNeill, V. F.; Laaksonen, A. Partitioning of Semivolatile Surface-Active Compounds between Bulk, Surface and Gas Phase. *Geophys. Res. Lett.* **2011**.
(36) Wren, S. N.; Valley, N. A.; Gordon, B. P.; McWilliams, L. E.; Richmond, G. L. Hydration, Orientation, and Conformation of Methylglyoxal at the Air-Water Interface. *J. Phys. Chem. A* **2015**, *119*, 6391−6403.
(37) Pocker, Y.; Meany, J. E.; Nist, B. J.; Zadorojny, C. Reversible Hydration of Pyruvic Acid. I. Equilibrium Studies. *J. Phys. Chem.* **1969**, *73*, 2879−2882.
(38) Betterton, E. A.; Hoffmann, M. R. Henry Law Constants of Some Environmentally Important Aldehydes. *Environ. Sci. Technol.* **1988**, *22*, 1415−1418.
(39) Sareen, N.; Schwier, A. N.; Shapiro, E. L.; Mitroo, D.; McNeill, V. F. Secondary Organic Material Formed by Methylglyoxal in Aqueous Aerosol Mimics. *Atmos. Chem. Phys.* **2010**, *10*, 997−1016.
(40) Casale, M. T.; Richman, A. R.; Elrod, M. J.; Garland, R. M.; Beaver, M. R.; Tolbert, M. A. Kinetics of Acid-Catalyzed Aldol Condensation Reactions of Aliphatic Aldehydes. *Atmos. Environ.* **2007**, *41*, 6212−6224.
(41) Renard, P.; Reed Harris, A. E.; Rapf, R. J.; Ravier, S.; Demelas, C.; Coulomb, B.; Quivet, E.; Vaida, V.; Monod, A. Aqueous Phase Oligomerization of Methyl Vinyl Ketone by Atmospheric Radical Reactions. *J. Phys. Chem. C* **2014**, *118*, 29421−29430.
(42) Schwier, A. N.; Sareen, N.; Mitroo, D.; Shapiro, E. L.; McNeill, V. F. Glyoxal-Methylglyoxal Cross-Reactions in Secondary Organic Aerosol Formation. *Environ. Sci. Technol.* **2010**, *44*, 6174−6182.
(43) Yu, G.; Bayer, A. R.; Galloway, M. M.; Korshavn, K. J.; Fry, C. G.; Keutsch, F. N. Glyoxal in Aqueous Ammonium Sulfate Solutions: Products, Kinetics, and Hydration Effects. *Environ. Sci. Technol.* **2011**, *45*, 6336−6342.
(44) Zhao, R.; Lee, A. K. Y.; Abbatt, J. P. D. Investigation of Aqueous-Phase Photooxidation of Glyoxal and Methylglyoxal by Aerosol Chemical Ionization Mass Spectrometry: Observation of Hydroxyhydroperoxide Formation. *J. Phys. Chem. A* **2012**, *116*, 6253−6263.
(45) Rapf, R. J.; Perkins, R. J.; Carpenter, B. K.; Vaida, V. Mechanistic Description of Photochemical Oligomer Formation from Aqueous Pyruvic Acid. *J. Phys. Chem. A* **2017**, *121*, 4272−4282.
(46) Donaldson, D. J.; Vaida, V. The Influence of Organic Films at the Air-Aqueous Boundary on Atmospheric Processes. *Chem. Rev.* **2006**, *106*, 1445−1461.
(47) Donaldson, D. J.; Valsaraj, K. T. Adsorption and Reaction of Trace Gas-Phase Organic Compounds on Atmospheric Water Film Surfaces: A Critical Review. *Environ. Sci. Technol.* **2010**, *44*, 865−873.
(48) Köhler, H. The Nucleus in the Growth of Hygroscopic Droplets. *Trans. Faraday Soc.* **1936**, *32*, 1152−1161.
(49) Prisle, N. L.; Asmi, A.; Topping, D.; Partanen, A. I.; Romakkaniemi, S.; Dal Maso, M.; Kulmala, M.; Laaksonen, A.; Lehtinen, K. E. J.; McFiggans, G. Surfactant Effects in Global Simulations of Cloud Droplet Activation. *Geophys. Res. Lett.* **2012**, *39*, L05802.
(50) Prisle, N. L.; Raatikainen, T.; Laaksonen, A.; Bilde, M. Surfactants in Cloud Droplet Activation: Mixed Organic-Inorganic Particles. *Atmos. Chem. Phys.* **2010**, *10*, 5663−5683.
(51) Sorjamaa, R.; Svenningsson, B.; Raatikainen, T.; Henning, S.; Bilde, M.; Laaksonen, A. The Role of Surfactants in Kohler Theory Reconsidered. *Atmos. Chem. Phys.* **2004**, *4*, 2107−2117.
(52) Rapf, R. J.; Dooley, M. R.; Kappes, K.; Perkins, R. J.; Vaida, V. pH Dependence of the Aqueous Photochemistry of α-Keto Acids. *J. Phys. Chem. A* **2017**, *121*, 8368−8379.
(53) Reed Harris, A. E.; Pajunoja, A.; Cazaunau, M.; Gratien, A.; Pangui, E.; Monod, A.; Griffith, E. C.; Virtanen, A.; Doussin, J.-F.; Vaida, V. Multiphase Photochemistry of Pyruvic Acid under Atmospheric Conditions. *J. Phys. Chem. A* **2017**, *121*, 3327−3339.
(54) Rodriguez, A. A.; de Loera, A.; Powelson, M. H.; Galloway, M. M.; De Haan, D. O. Formaldehyde and Acetaldehyde Increase Aqueous-Phase Production of Imidazoles in Methylglyoxal/Amine Mixtures: Quantifying a Secondary Organic Aerosol Formation Mechanism. *Environ. Sci. Technol. Lett.* **2017**, *4*, 234−239.
(55) Shrivastava, M.; Cappa, C. D.; Fan, J.; Goldstein, A. H.; Guenther, A. B.; Jimenez, J. L.; Kuang, C.; Laskin, A.; Martin, S. T.; Ng, N. L.; et al. Recent Advances in Understanding Secondary Organic Aerosol: Implications for Global Climate Forcing. *Rev. Geophys.* **2017**, *55*, 509−559.

DOI: 10.1021/acs.jpca.8b01193
J. Phys. Chem. A 2018, 122, 3837−3849

(56) Ortiz-Montalvo, D. L.; Hakkinen, S. A. K.; Schwier, A. N.; Lim, Y. B.; McNeill, V. F.; Turpin, B. J. Ammonium Addition (and Aerosol pH) Has a Dramatic Impact on the Volatility and Yield of Glyoxal Secondary Organic Aerosol. *Environ. Sci. Technol.* **2014**, *48*, 255−262.
(57) Bell, S. Ab Initio Study of the Barriers to Methyl Torsion and Torsional Frequencies of Acetyl Molecules. *Spectrochim. Acta, Part A* **2005**, *61*, 1471−1477.
(58) Braakman, R.; Drouin, B. J.; Widicus Weaver, S. L.; Blake, G. A. Extended Analysis of Hydroxyacetone in the Torsional Ground State. *J. Mol. Spectrosc.* **2010**, *264*, 43−49.
(59) Jetzki, M.; Luckhaus, D.; Signorell, R. Fermi Resonance and Conformation in Glycolaldehyde Particles. *Can. J. Chem.* **2004**, *82*, 915−924.
(60) Kattija-Ari, M.; Harmony, M. D. The Microwave Spectrum and Conformation of Hydroxyacetone: The Influence of Hydrogen Bonding on the Barrier to Internal Rotation of the Methyl Group. *Int. J. Quantum Chem.* **1980**, *18*, 443−453.
(61) Lasne, J.; Laffon, C.; Parent, P. Interaction of Acetone, Hydroxyacetone, Acetaldehyde and Benzaldehyde with the Surface of Water Ice and HNO_3•$3H_2O$ Ice. *Phys. Chem. Chem. Phys.* **2012**, *14*, 697−704.
(62) Lindenmaier, R.; Tipton, N.; Sams, R. L.; Brauer, C. S.; Blake, T. A.; Williams, S. D.; Johnson, T. J. Assignment of the Fundamental Modes of Hydroxyacetone Using Gas-Phase Infrared, Far-Infrared, Raman, and ab Initio Methods: Band Strengths for Atmospheric Measurements. *J. Phys. Chem. A* **2016**, *120*, 5993−6003.
(63) Mohaček-Grošev, V. Vibrational Analysis of Hydroxyacetone. *Spectrochim. Acta, Part A* **2005**, *61*, 477−484.
(64) Petitjean, M.; Darvas, M.; Picaud, S.; Jedlovszky, P.; Le Calve, S. Adsorption of Hydroxyacetone on Pure Ice Surfaces. *ChemPhysChem* **2010**, *11*, 3921−3927.
(65) Sharma, A.; Reva, I.; Fausto, R. Matrix-insolation Study and Ab Initio Calculations of the Structure and Spectra of Hydroxyacetone. *J. Phys. Chem. A* **2008**, *112*, 5935−5946.
(66) Sharma, A.; Reva, I.; Fausto, R. Conformational Switching Induced by Near-infrared Laser Irradiation. *J. Am. Chem. Soc.* **2009**, *131*, 8752−8753.
(67) Sharma, A.; Reva, I.; Fausto, R.; Hesse, S.; Xue, Z.; Suhm, M. A.; Nayak, S. K.; Sathishkumar, R.; Pal, R.; Guru Row, T. N. Conformation-changing Aggregation in Hydroxyacetone: A Combined Low-temperature FTIR, Jet, and Crystallographic Study. *J. Am. Chem. Soc.* **2011**, *133*, 20194−20207.
(68) Glushonok, G. K.; Glushonok, T. G.; Maslovskaya, L. A.; Shadyro, O. I. A ^{1}H and ^{13}C NMR and UV Study of the State of Hydroxyacetone in Aqueous Solutions. *Russ. J. Gen. Chem.* **2003**, *73*, 1027−1031.
(69) Dutta, C.; Benderskii, A. V. On the Assignment of the Vibrational Spectrum of the Water Bend at the Air/Water Interface. *J. Phys. Chem. Lett.* **2017**, *8*, 801−804.
(70) Eisenthal, K. B. Liquid Interfaces Probed by Second-Harmonic and Sum-Frequency Spectroscopy. *Chem. Rev.* **1996**, *96*, 1343−1360.
(71) Feng, R. R.; Guo, Y.; Lü, R.; Velarde, L.; Wang, H. F. Consistency in the Sum Frequency Generation Intensity and Phase Vibrational Spectra of the Air/Neat Water Interface. *J. Phys. Chem. A* **2011**, *115*, 6015−6027.
(72) Lambert, A. G.; Davies, P. B.; Neivandt, D. J. Implementing the Theory of Sum Frequency Generation Vibrational Spectroscopy: A Tutorial Review. *Appl. Spectrosc. Rev.* **2005**, *40*, 103−145.
(73) Morita, A.; Hynes, J. T. A Theoretical Analysis of the Sum Frequency Generation Spectrum of the Water Surface. *Chem. Phys.* **2000**, *258*, 371−390.
(74) Perakis, F.; De Marco, L.; Shalit, A.; Tang, F.; Kann, Z. R.; Kühne, T. D.; Torre, R.; Bonn, M.; Nagata, Y. Vibrational Spectroscopy and Dynamics of Water. *Chem. Rev.* **2016**, *116*, 7590−7607.
(75) Richmond, G. L. Molecular Bonding and Interactions at Aqueous Surfaces as Probed by Vibrational Sum Frequency Spectroscopy. *Chem. Rev.* **2002**, *102*, 2693−2724.
(76) Schaefer, J.; Backus, E. H. G.; Nagata, Y.; Bonn, M. Both Inter- and Intramolecular Coupling of O−H Groups Determine the Vibrational Response of the Water/Air Interface. *J. Phys. Chem. Lett.* **2016**, *7*, 4591−4595.
(77) Shen, Y. R. Basic Theory of Surface Sum-Frequency Generation. *J. Phys. Chem. C* **2012**, *116*, 15505−15509.
(78) Tian, C. S.; Shen, Y. R. Sum-Frequency Vibrational Spectroscopic Studies of Water/Vapor Interfaces. *Chem. Phys. Lett.* **2009**, *470*, 1−6.
(79) Verreault, D.; Hua, W.; Allen, H. C. From Conventional to Phase-Sensitive Vibrational Sum Frequency Generation Spectroscopy: Probing Water Organization at Aqueous Interfaces. *J. Phys. Chem. Lett.* **2012**, *3*, 3012−3028.
(80) Lu, R.; Gan, W.; Wu, B. H.; Zhang, Z.; Guo, Y.; Wang, H. F. C−H Stretching Vibrations of Methyl, Methylene and Methine Groups at the Vapor/Alcohol (n = 1−8) Interfaces. *J. Phys. Chem. B* **2005**, *109*, 14118−14129.
(81) Ishiyama, T.; Imamura, T.; Morita, A. Theoretical Studies of Structures and Vibrational Sum Frequency Generation Spectra at Aqueous Interfaces. *Chem. Rev.* **2014**, *114*, 8447−8470.
(82) Bain, C. D.; Davies, P. B.; Ong, T. H.; Ward, R. N.; Brown, M. A. Quantitative Analysis of Monolayer Composition by Sum-Frequency Vibrational Spectroscopy. *Langmuir* **1991**, *7*, 1563−1566.
(83) Moore, F. G.; Becraft, K. A.; Richmond, G. L. Challenges in Interpreting Vibrational Sum Frequency Spectra: Deconvoluting Spectral Features as Demonstrated in the Calcium Fluoride-Water-Sodium Dodecylsulfate System. *Appl. Spectrosc.* **2002**, *56*, 1575−1578.
(84) Chieffo, L.; Shattuck, J.; Amsden, J. J.; Erramilli, S.; Ziegler, L. D. Ultrafast Vibrational Relaxation of Liquid H_2O Following Librational Combination Band Excitation. *Chem. Phys.* **2007**, *341*, 71−80.
(85) Knop, S.; Lindner, J.; Vöhringer, P. OH and NH Stretching Vibrational Relaxation of Liquid Ethanolamine. *Z. Phys. Chem.* **2011**, *225*, 913−926.
(86) Monson, P. R.; Patumtevapibal, S.; Kaufmann, K. J.; Robinson, G. W. Dominance of Methyl-Groups in Picosecond Vibrational-Relaxation in Hydrocarbons. *Chem. Phys. Lett.* **1974**, *28*, 312−315.
(87) Nienhuys, H. K.; van Santen, R. A.; Bakker, H. J. Orientational Relaxation of Liquid Water Molecules as an Activated Process. *J. Chem. Phys.* **2000**, *112*, 8487−8494.
(88) Woutersen, S.; Emmerichs, U.; Bakker, H. J. Femtosecond mid-IR pump-probe spectroscopy of liquid water: Evidence for a two-component structure. *Science* **1997**, *278*, 658−660.
(89) McWilliams, L. E.; Valley, N. A.; Vincent, N. M.; Richmond, G. L. Interfacial Insights into a Carbon Capture System: CO_2 Uptake to an Aqueous Monoethanolamine Surface. *J. Phys. Chem. A* **2017**, *121*, 7956−7967.
(90) McWilliams, L. E.; Valley, N. A.; Wren, S. N.; Richmond, G. L. A Means to an Interface: Investigating Monoethanolamine Behavior at an Aqueous Surface. *Phys. Chem. Chem. Phys.* **2015**, *17*, 21458−21469.
(91) Davies, J. T.; Rideal, E. K. *Interfacial Phenomena*; Academic Press: New York, 1963.
(92) Blower, P. G.; Ota, S. T.; Valley, N. A.; Wood, S. R.; Richmond, G. L. Sink or Surf: Atmospheric Implications for Succinic Acid at Aqueous Surfaces. *J. Phys. Chem. A* **2013**, *117*, 7887−7903.
(93) Plath, K. L.; Valley, N. A.; Richmond, G. L. Ion-Induced Reorientation and Distribution of Pentanone in the Air−Water Boundary Layer. *J. Phys. Chem. A* **2013**, *117*, 11514−11527.
(94) Valley, N. A.; Richmond, G. L. Solvation Station: Micro-solvation for Modeling Vibrational Sum-Frequency Spectra of Acids at Aqueous Interfaces. *J. Chem. Theory Comput.* **2015**, *11*, 4780−4790.
(95) Valley, N. A.; Richmond, G. L. Computational Vibrational Sum Frequency Spectra of Formaldehyde and Hydroxymethanesulfonate at Aqueous Interfaces. *J. Phys. Chem. C* **2016**, *120*, 14122−14129.
(96) Valley, N. A.; Robertson, E. J.; Richmond, G. L. Twist and Turn: Effect of Stereoconfiguration on the Interfacial Assembly of Polyelectrolytes. *Langmuir* **2014**, *30*, 14226−14233.
(97) Valley, N. V.; Blower, P. G.; Wood, S. R.; Plath, K. L.; McWilliams, L. E.; Richmond, G. L. Doubling Down: Delving into the

DOI: 10.1021/acs.jpca.8b01193
J. Phys. Chem. A 2018, 122, 3837−3849

Details of Diacid Adsorption at Aqueous Surfaces. *J. Phys. Chem. A* **2014**, *118*, 4778−4789.
(98) Case, D. A.; Darden, T. A.; Cheatham, T. E.; Simmerling, C. L.; Wang, J.; Duke, R. E.; Luo, R.; Walker, R. C.; Zhang, W.; Merz, K. M. Amber 12; University of California: San Francisco, 2012.
(99) Martinez, L.; Andrade, R.; Birgin, E.; Martinez, J. Packmol: A Package for Building Initial Configurations for Molecular Dynamics Simulations. *J. Comput. Chem.* **2009**, *30*, 2157−2164.
(100) Frisch, M. J.; Trucks, G. W.; Schlegel, H. B.; Scuseria, G. E.; Robb, M. A.; Cheeseman, J. R.; Scalmani, G.; Barone, V.; Mennucci, B.; Petersson, G. A.; et al. *Gaussian 09*; Gaussian Inc.: Wallingford, CT, 2009.
(101) Nagata, Y.; Hsieh, C. S.; Hasegawa, T.; Voll, J.; Backus, E. H. G.; Bonn, M. Water Bending Mode at the Water−Vapor Interface Probed by Sum-Frequency Generation Spectroscopy: A Combined Molecular Dynamics Simulation and Experimental Study. *J. Phys. Chem. Lett.* **2013**, *4*, 1872−1877.
(102) Ni, Y.; Skinner, J. L. IR and SFG Vibrational Spectroscopy of the Water Bend in the Bulk Liquid and at the Liquid-Vapor Interface, Respectively. *J. Chem. Phys.* **2015**, *143* (1), 014502.
(103) Vinaykin, M.; Benderskii, A. V. Vibrational Sum-Frequency Spectrum of the Water Bend at the Air/Water Interface. *J. Phys. Chem. Lett.* **2012**, *3*, 3348−3352.
(104) Rosen, M. J. In *Surfactants and Interfacial Phenomena*, 3rd ed.; John Wiley & Sons, Inc.: New York, 2004.

DOI: 10.1021/acs.jpca.8b01193
J. Phys. Chem. A 2018, 122, 3837−3849